Supporting Information

Table S1. Comparisons of the synthesis details and electrochemical performance with serial carbonaceous sulfur hosts in lithium-sulfur batteries.

Host	Sulfur loading($mg \cdot cm^{-2}$) or content (wt%)	Areal Capacity ($mAh \cdot cm^{-2}$)	Capacity ($mAh \cdot g^{-1}$)	Rate (C)	Electrolyte/sulfur ratio ($\mu L \cdot mg^{-1}$)	Ref.
Co-NCFs	4.2 / 75	4.5	1071	0.5	15	[1]
NbC/Co-CFs	1.5 / 80	2.2	1466	0.1	10	[2]
VN-NC	7.1 / 75	4.8	676	0.05	10	[3]
MoN-C	1.2 / 75	1.92	1600	0.2	6.5	[4]
ePCNTM-20	2.0 / 75	2.13	1065	0.1	15	[5]
Fe_2N_{1-x}-NCT_{25}	5.1 / 90	5.26	1031	0.1	10	This work
Fe_2N_{1-x}-NCT_{25}	5.1 / 90	4.19	821	0.1	8	This work
Fe_2N_{1-x}-NCT_{25}	5.1 / 90	3.38	662	0.1	5	This work

Table S2: The detailed content of various sulfur contained cathode in this work.

Cathode	Sulfur	Host	PVDF binder	Aluminum foil (Φ=12mm)
NCT_{25}	2.26 mg	0.96 mg	0.36 mg	4.83 mg
Fe_2N_{1-x}-NCT_{15}	2.31 mg	0.99 mg	0.37 mg	
Fe_2N_{1-x}-NCT_{20}	2.23 mg	0.95 mg	0.35 mg	
Fe_2N_{1-x}-NCT_{25}	2.35 mg	1.00 mg	0.37 mg	
High-loading Fe_2N_{1-x}-NCT_{25}	5.76 mg	0.64 mg	0.71 mg	

Table S3: Summary of textural parameters of the obtained Fe_2N_{1-x}-NCT samples.

Samples	S_{BET} ($m^2\ g^{-1}$)	S_{Meso} ($m^2\ g^{-1}$)	S_{Micro} ($m^2\ g^{-1}$)	V_t ($cm^3\ g^{-1}$)	V_{Meso} ($cm^3\ g^{-1}$)	V_{micro} ($cm^3\ g^{-1}$)
Fe_2N_{1-x}-NCT_{15}	120	21	99	0.20	0.12	0.08
Fe_2N_{1-x}-NCT_{20}	263	161	102	0.25	0.15	0.10
Fe_2N_{1-x}-NCT_{25}	312	202	110	0.30	0.19	0.11

S_{BET}: total BET specific surface area, S_{Meso}: mesopore specific surface area, S_{Micro}: micropore specific surface area, V_t: total pore volume, V_{Meso}: mesoporous volume, V_{Micro}: microporous volume.

Table S4: Summarized XPS data for polystyrene-ferrocene/polydopamine-Fe^{3+} (PS-Fe/PDA-Fe^{3+}) fibers in Fig. S2a. Fe 2p binding energies (eV) for selected iron species are provided.

Samples	Sat.	Porphyrin Fe $2p_{1/2}$	Sat.	Porphyrin Fe $2p_{3/2}$
PS-Fe/PDA-Fe^{3+} fibers	727.8	723.7	715.4	710.8

Table S5: Summarized XPS data for NCT_{25} and Fe_2N_{1-x}-NCT_{25} in Fig. 3e. N 1s binding energies (eV) for selected nitrogen species are provided.

Samples	Oxided N	Graphite N	Pyrrole N	Fe-N	Pyridinic N
Fe_2N_{1-x}-NCT_{25}	402.8	401.1	400.0	398.6	398.0
NCT_{25}	402.8	401.2	400.2	/	398.2

Table S6: Summarized XPS data for Fe_2N_{1-x}-NCT_{25} in Fig. 3f. Fe 2p binding energies (eV) for selected iron species at different depth are provided.

Samples	Sat.	Fe^{2+} $2p_{1/2}$	Fe^0 $2p_{1/2}$	Sat.	Fe^{2+} $2p_{3/2}$	Fe^0 $2p_{3/2}$	Fe/N
Surface of Fe_2N_{1-x}-NCT_{25}	727.0	725.1	722.2	400.0	716.8	709.1	1.98
50 nm depth of of Fe_2N_{1-x}-NCT_{25}	726.9	724.8	/	400.2	715.5	/	1.74

Table S7: Summarized XPS data for NCT_{25}/Li_2S_6 in Fig. 4e. S 2p binding energies (eV) for selected sulfur species are provided.

Samples	Sulfate	S_B^0	S_T^{-1}
Blank	/	164.6/163.6	163.2/162.3
NCT_{25}	168.5/166.7	164.4/163.9	163.2/162.7

Table S8: Summarized XPS data for Fe_2N_{1-x}-NCT_{25}/Li_2S_6 in Fig. 4f. S 2p binding energies (eV) for selected sulfur species are provided.

Samples	Sulfate	S_B^0	S_T^{-1}
Blank	/	164.6/163.6	163.2/162.3
Fe_2N_{1-x}-NCT_{25}	168.7/166.9	165.0/164.1	163.7/163.3

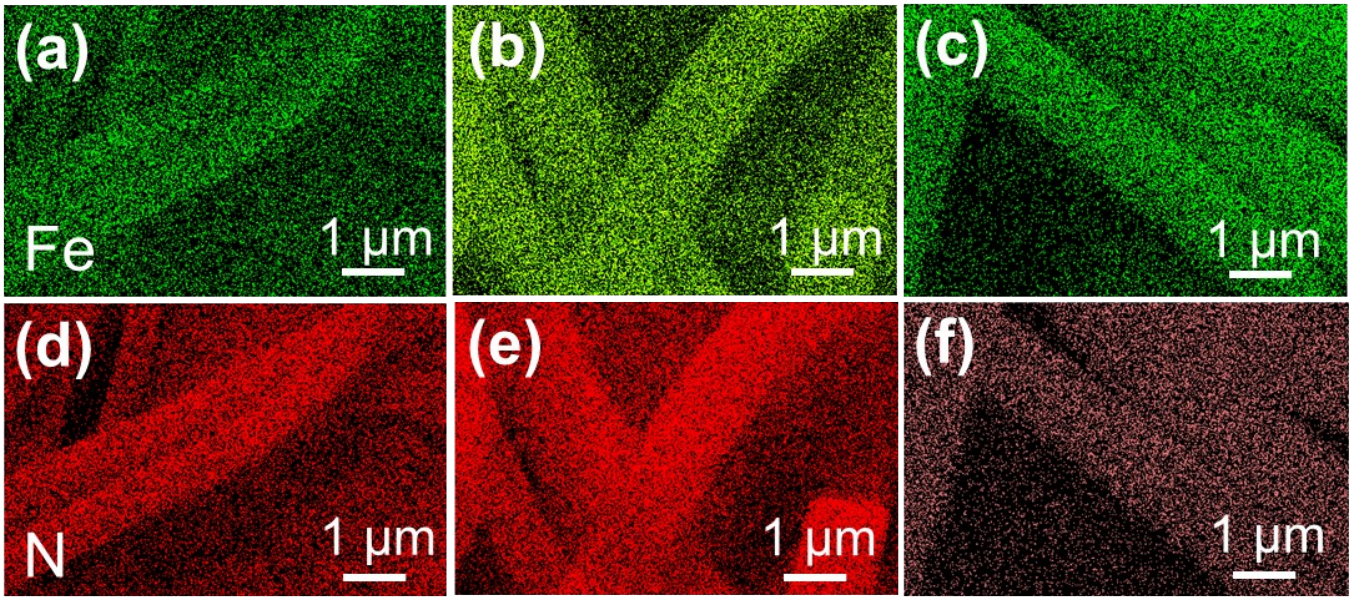

Figure S1. Corresponding elemental mapping images of Figure 1b, 1f, and 1j.

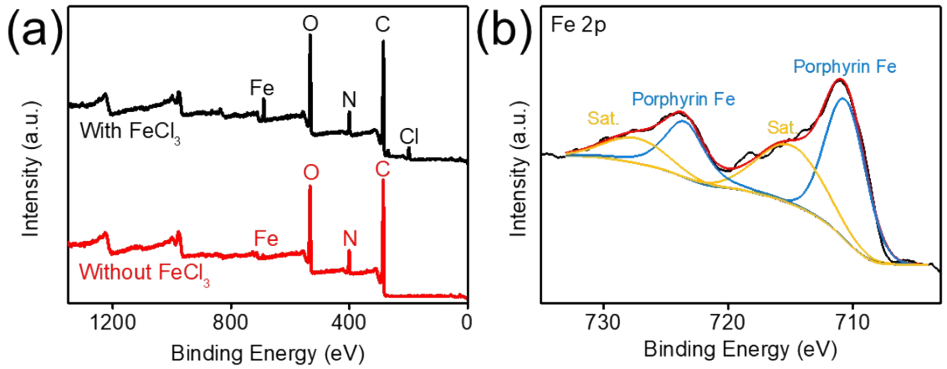

Figure S2. (a) The XPS survey spectra and the high-resolution XPS spectra of (b) Fe 2p for polystyrene-ferrocene/polydopamine-Fe^{3+} fibers.

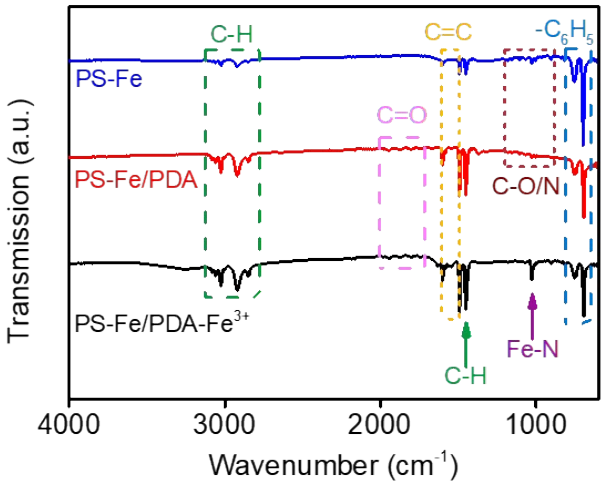

Figure S3. FT-IR patterns of polystyrene-ferrocene fibers, polystyrene-ferrocene/polydopamine fibers, and polystyrene-ferrocene/polydopamine-Fe^{3+} fibers.

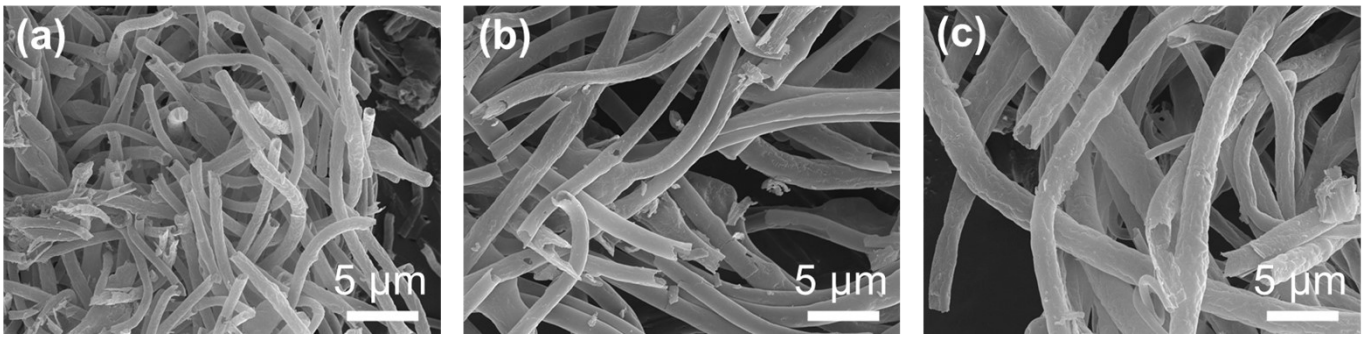

Figure S4. Low-magnification SEM images of Fe_2N_{1-x}-NCT samples at a polystyrene concentration of (a) 15 wt%, (b) 20 wt%, and (c) 25 wt%.

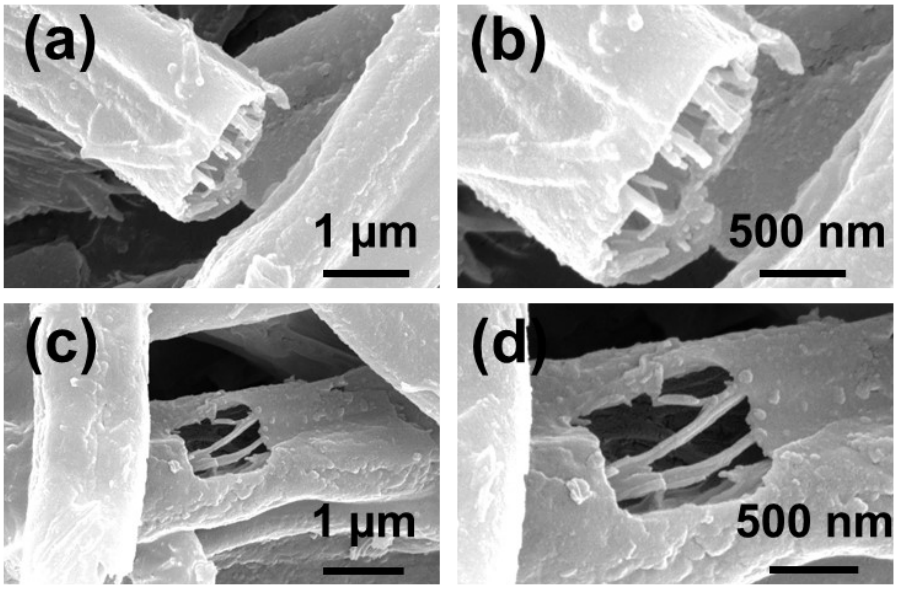

Figure S5. High-magnification SEM images of Fe_2N_{1-x}-NCT_{25} samples at a polystyrene concentration of 25 wt%.

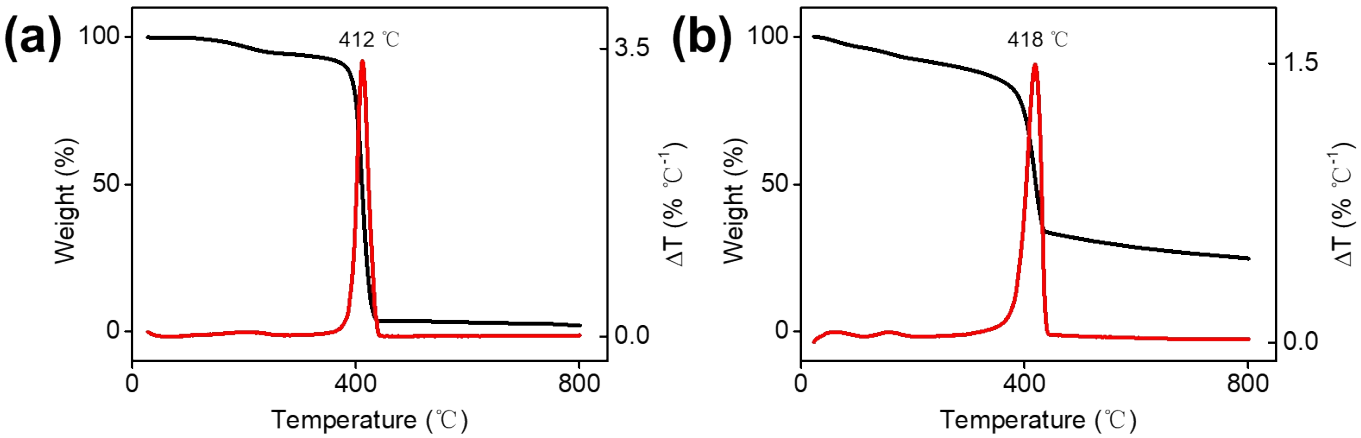

Figure S6. TG/DSC curves of (a) polystyrene-ferrocene fibers and (b) polystyrene-ferrocene/polydopamine-Fe^{3+} fibers.

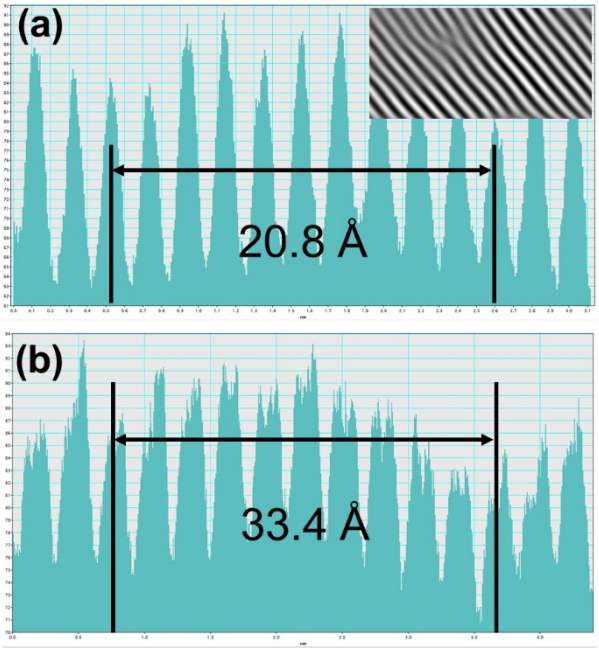

Figure S7. The IFFT patterns of (a) Fe_2N_{1-x} nanocrystal and (b) graphene layer.

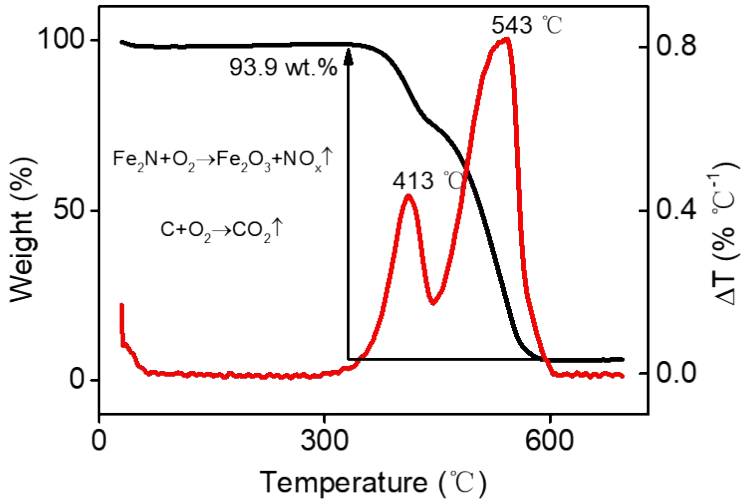

$$W(Fe_2O_3)= 100\%-W(C)=6.1\ \%$$

$$W(Fe_2N)= \frac{M(Fe_2N)}{M(Fe_2O_3)} \cdot W(Fe_2O_3)=4.8\ \%$$

Figure S8. TG/DSC curves of Fe_2N_{1-x}-NCT_{25} sample.

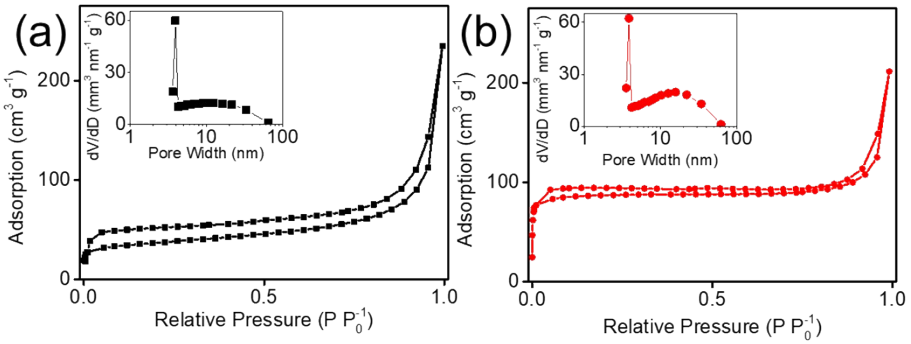

Figure S9. N_2 adsorption/desorption isotherm curve and pore distribution (inset) of (a) Fe_2N_{1-x}-NCT_{15} and (b) Fe_2N_{1-x}-NCT_{20}.

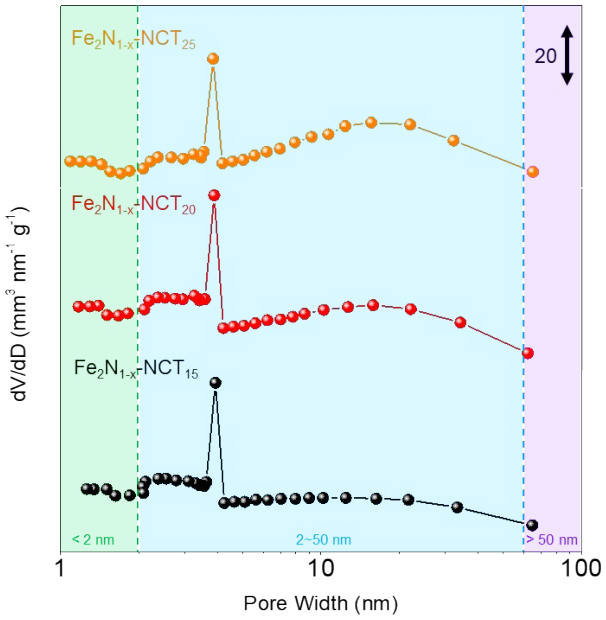

Figure S10. Pore size distribution of Fe_2N_{1-x}-NCT of different diameters.

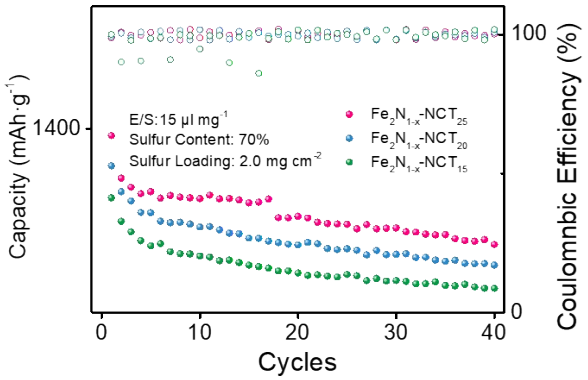

Figure S11. Cycling performances at 0.1 C of LSBs with Fe_2N_{1-x}-NCT hosts (with raised polystyrene concentration) under sulfur loading of 2.0 mg·cm^{-2}.

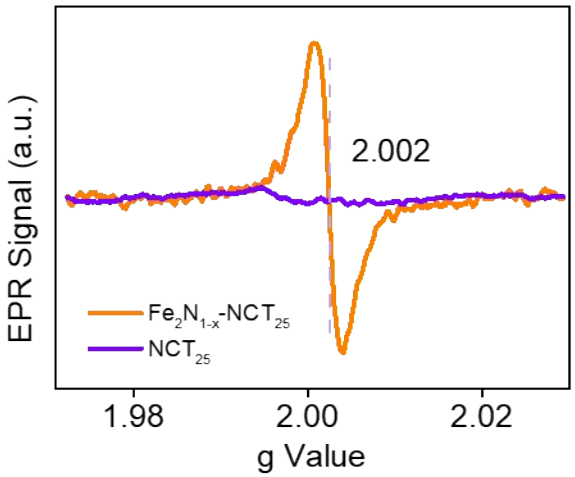

Figure S12. EPR pattern of Fe_2N_{1-x}-NCT_{25} and NCT_{25}.

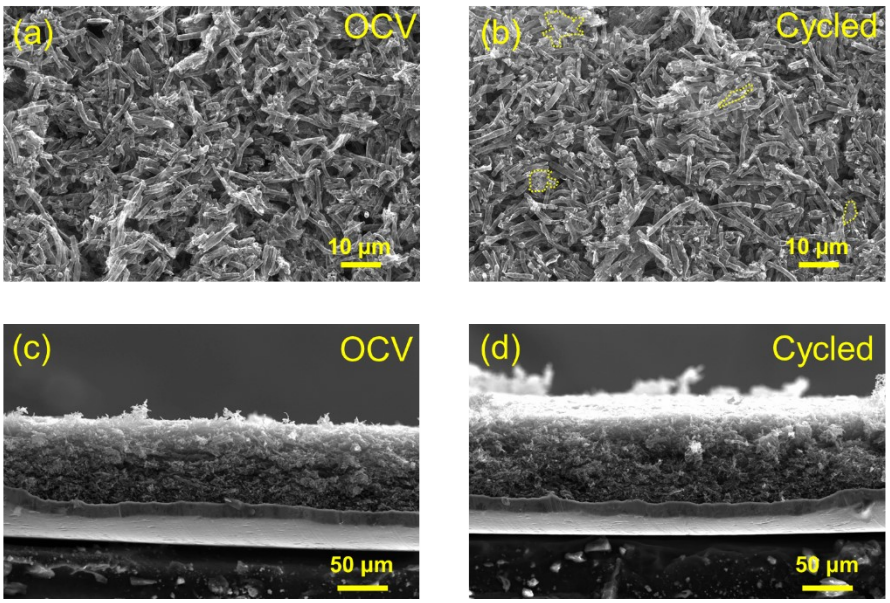

Figure S13. SEM images of (a) fresh Fe_2N_{1-x}-NCT_{25}/S cathode and (b) cycled Fe_2N_{1-x}-NCT_{25}/S cathode, cross-section SEM images of (c) fresh Fe_2N_{1-x}-NCT_{25}/S cathode and (d) cycled Fe_2N_{1-x}-NCT_{25}/S cathode. (Observable sulfur particles in yellow circles).

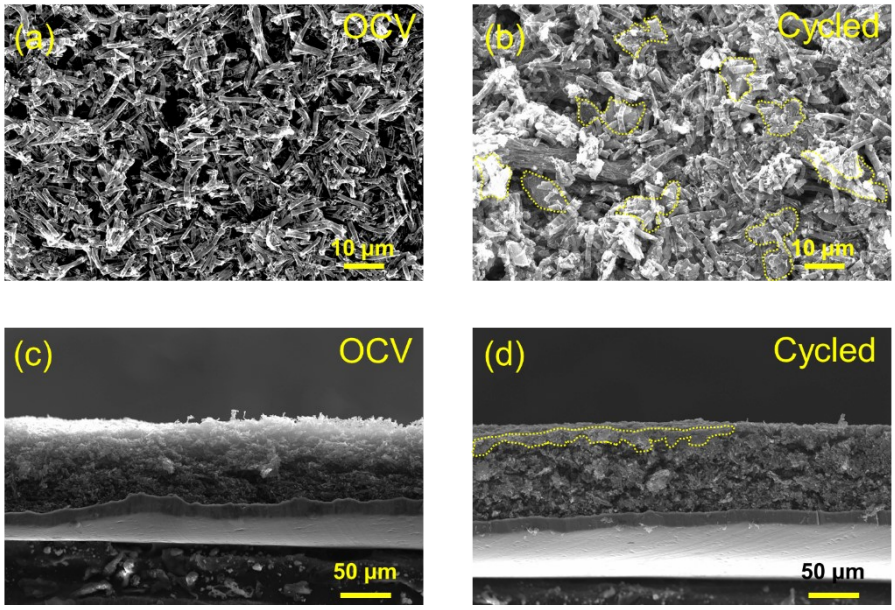

Figure S14. SEM images of (a) fresh NCT_{25}/S cathode and (b) cycled NCT_{25}/S cathode, cross-section SEM images of (c) fresh NCT_{25}/S cathode and (d) cycled NCT_{25}/S cathode. (Observable sulfur particles in yellow circles).

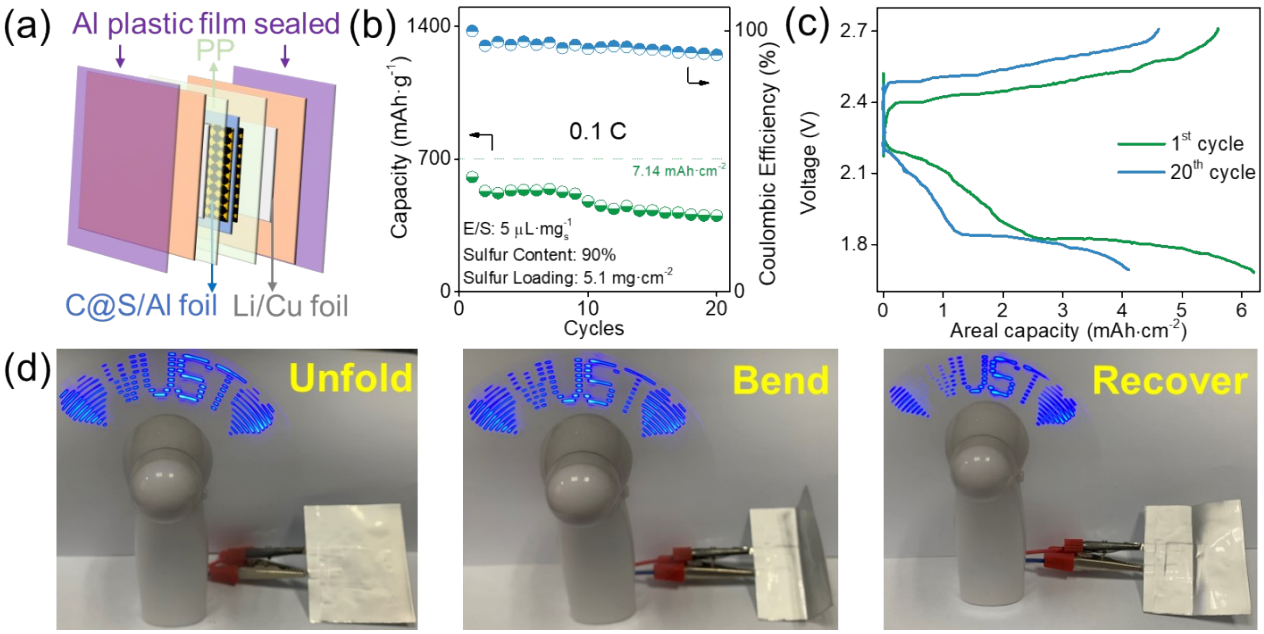

Figure S15. (a) Assembling scheme of a Li-S punch cell. (b) Cycling performance and (c) voltage profiles of the Fe_2N_{1-x}-NCT_{25}/S cathode assembled punch cell at 0.1 C. (d) A Li-S punch cell supported LED fan worked when cell was unfolded (left), bended (middle), and recovered (right).

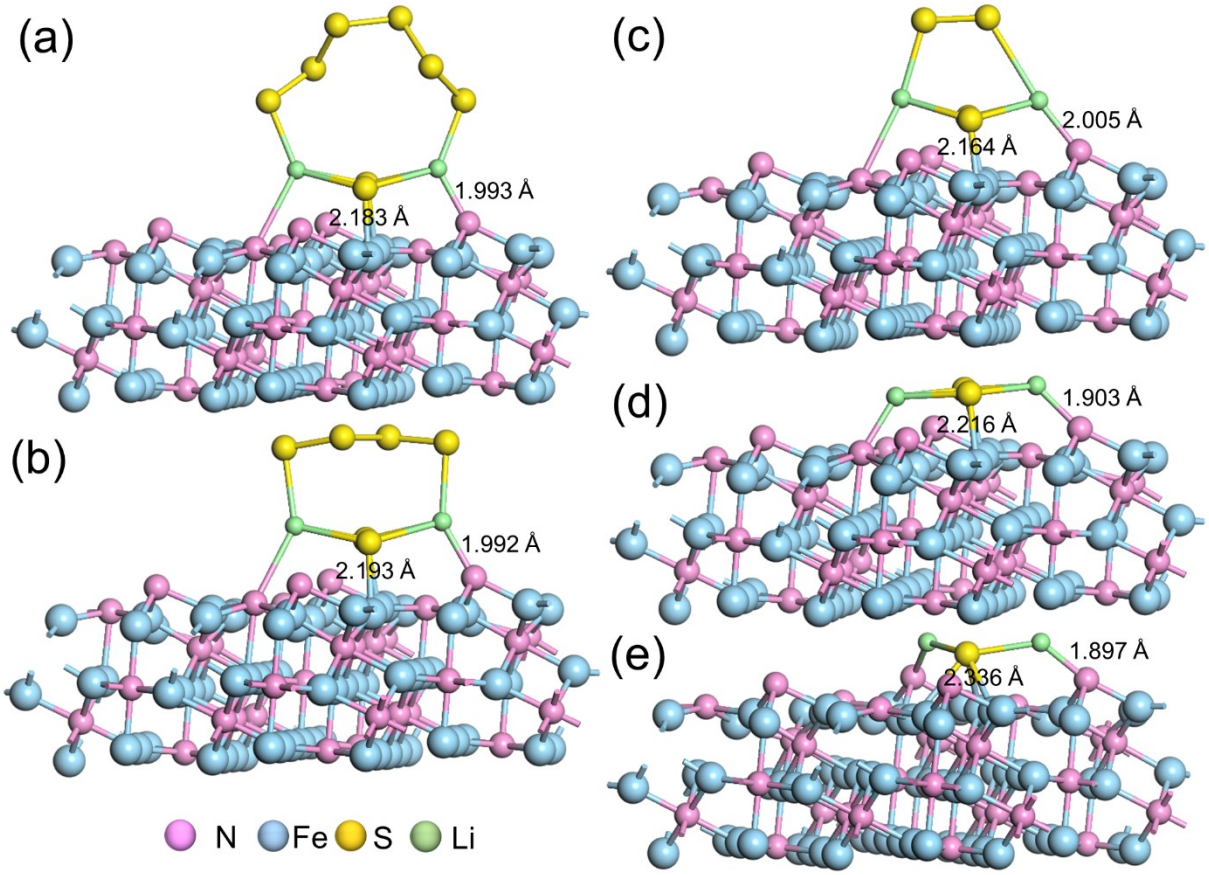

Figure S16. DFT calculation results of optimized geometrical configurations of (a) Li_2S_8, (b) Li_2S_6, (c) Li_2S_4, (d) Li_2S_2, (e) Li_2S molecules on the nitrogen deficient Fe_2N_{1-x} ($\bar{1}\bar{1}0$) surface model.

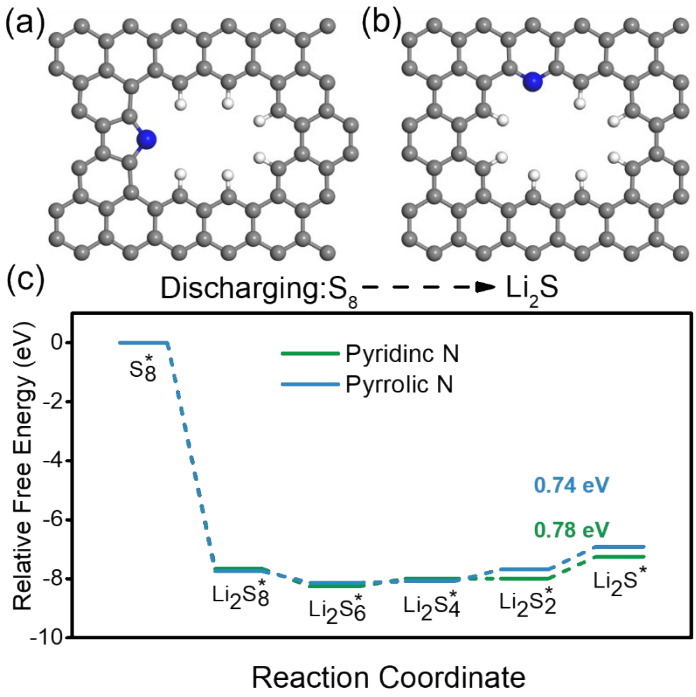

Figure S17. Structures of (a) pyrrolic N-doped and (b) pyridinic N-doped NCT used in first-principles calculations. The white, grey, yellow, blue, and purple balls represent H, C, N, and Li atoms, respectively. (c) Free energy diagrams for the reduction of LiPSs near the pyrrolic N and pyridinic N defects.

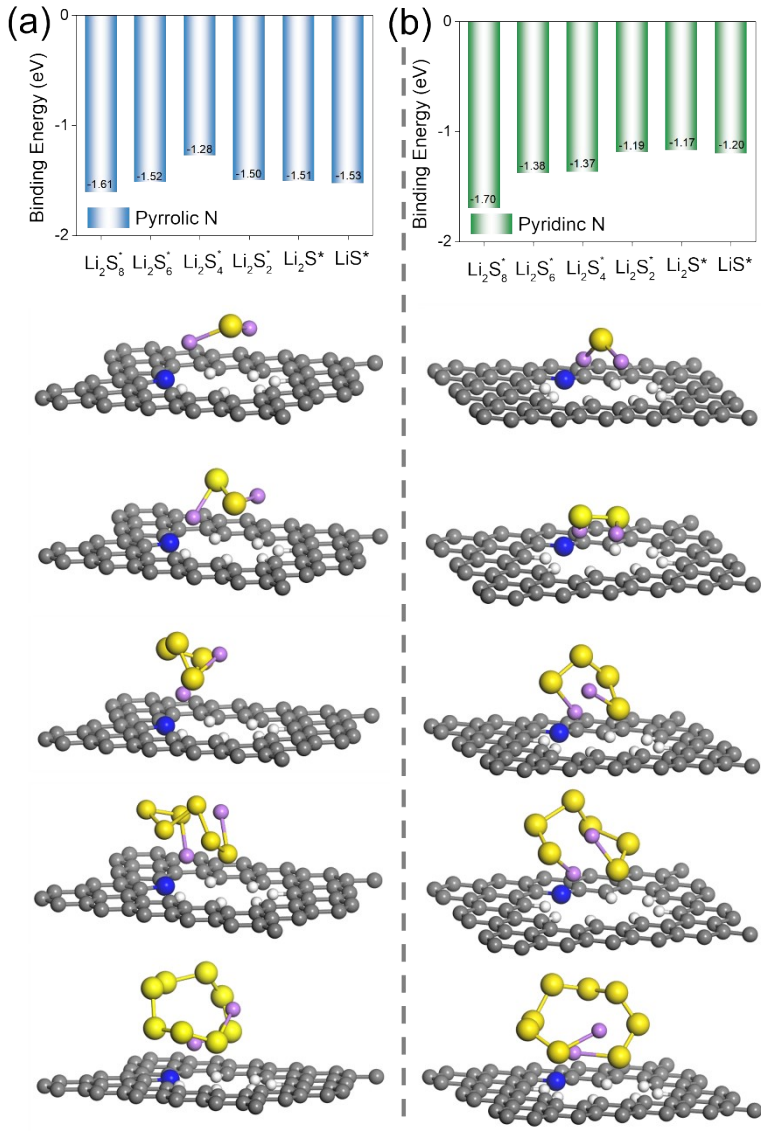

Figure S18. Adsorption energy of LiPSs on (a) pyrrolic N-doped or (b) pyridinic N-doped NCT. Geometrically stable configurations of Li_2S, Li_2S_2, Li_2S_4, Li_2S_6, and Li_2S_8 on pyridinic N-doped or pyrrolic N-doped NCT (from up to down).

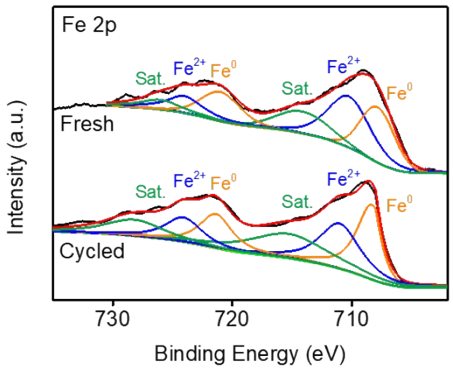

Figure S19. The high-resolution XPS spectra of Fe 2p for Fe_2N_{1-x}-NCT_{25} sample before and after cell cycling.

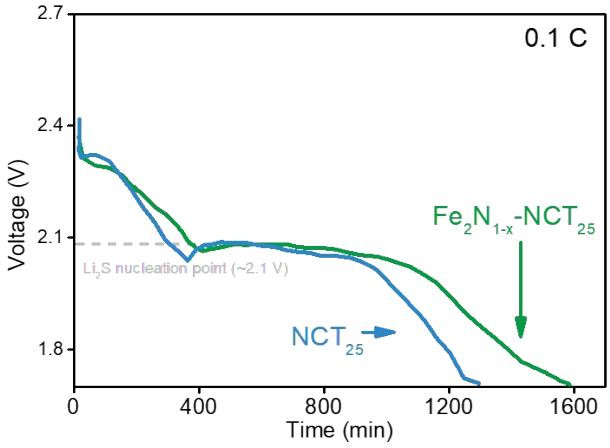

Figure S20. The voltage profiles of Fe_2N_{1-x}-NCT_{25}/S cathode and NCT_{25}/S cathode at 0.1 C for discharging.

References

[1] Y. Boyjoo, H. Shi, E. Olsson, *Adv. Energy Mater.* 2020, **10**, 2000651.
[2] Y. Wei, B. Wang, Y. Zhang, *Adv. Funct. Mater.* 2021, **31**, 2006033.
[3] X. Wang, D. Luo, J. Wang, *Angew. Chem. Int. Ed.* 2021, **60**, 2371-2378.
[4] R. Li, H. Peng, Q. Wu, *Angew. Chem. Int. Ed.* 2020, **59**, 12129-12138.
[5] Y. Zhang, G. Li, J. Wang, *Adv. Energy Mater.* 2021, **11**, 2100497